Theranostic Near Infrared-Active Conjugated Polymer Nanoparticles

Miao Zhao[1], Edward Leggett[1], Struan Bourke[1], Souzana Poursanidou[2], Sadie Carter-Searjeant[1], Steve Po[1], Marciano Palma do Carmo[1], Lea Ann Dailey[3], Philip Manning[4], Sean G. Ryan[5,6], Laura Urbano[2], Mark A. Green[1,]*, Aliaksandra Rakovich[1,]*

1. King's College London, Physics Department, Strand Building, London, WC2R 2LS, UK.

2. University of Hertfordshire, Department of Clinical, Pharmaceutical and Biological Sciences, College Lane, Hatfield, Hertfordshire, AL10 9AB, UK.

3. University of Vienna, Department of Pharmaceutical Technology and Biopharmacy, Vienna, Wien 1090, Austria.

4. Newcastle University, Translational and Clinical Research Institute, Faculty of Medical Sciences, Newcastle upon Tyne, Tyne and Wear, NE2 4HH, UK.

5. University of Hertfordshire, Department of Physics, Astronomy and Mathematics, College Lane, Hatfield, Hertfordshire, AL10 9AB, UK.

6. University College London, Centre for Advanced Biomedical Imaging, Gower Street, London, WC1E 6BT, UK.

ABSTRACT: Conjugated polymer nanoparticles (CPNs) based on a common solar cell material (PTB7) have been prepared, and their potential in theranostic applications based on bioimaging and photosensitizing capabilities has been evaluated. The main absorption and emission bands of the prepared CPN particles both fell within the NIR-I (650-950 nm) transparency window, allowing facile and efficient implementation of our CPNs as bioimaging agents, as demonstrated in this work for A549 human lung cancer cell cultures. The prepared CPN samples were also shown to produce reactive oxygen species (ROS) upon photoexcitation in the near infrared or ultraviolet spectral regions, both in aqueous solutions and in HaCaT keratinocyte cell cultures. Importantly, we show that the photosensitizing ability of our CPNs was largely determined by the nature of the stabilizing shell: coating the CPNs with a pluronic F127 copolymer led to an improvement of photoinitiated ROS production, while using PSMA instead completely quenched said process. This work therefore demonstrates that the photosensitizing capability of CPNs can be modulated *via* an appropriate selection of stabilizing material, and highlights the significance of this parameter for the on-demand design of theranostic probes based on CPNs.

KEYWORDS: conjugated polymer nanoparticles, theranostic probe, NIR-I, reactive oxygen species, photodynamic therapy

Photodynamic therapy (PDT) is a treatment method that relies on a photo-induced generation of reactive oxygen species by a photosensitizer (PS). When applied to cancer therapy, PDT has many advantages compared to conventional cancer treatments such as chemotherapy, surgery and radiation, which include a minimal invasiveness or damage to healthy tissues, lack of drug resistance, and appropriateness to a broad spectrum of cancer targets.[1–3] It is highly desirable to develop biocompatible photosensitizers with excellent ROS generation ability, and strong

near-infrared (NIR) absorption as NIR wavelengths experience less absorption and scattering in tissues,[4-6] leading to a deeper activation of the PDT. Nanomaterials are promising photosensitizers because of the advantageous properties that they offer. This includes the enhanced permeability and retention effect (EPR), which promotes nanomaterial accumulation in pathologically relevant areas.[7] However, many nanomaterials have intrinsic problems as photosensitizers: quantum dots (QDs) have excellent optical properties, but many are made from toxic heavy metals;[8] gold nanoparticles have better biocompatibility than QDs, but most absorb in the less favourable UV-Vis region.[9]

In contrast, conjugated polymer nanoparticles (CPNs) that comprise large pi-conjugated backbones and delocalized electronic structure, have attracted much attention because of their inherent photostability, high fluorescence brightness, visible or NIR emission, excellent biocompatibility, and compositions which are free from heavy metal ions.[10-15] As such they present distinct advantages over existing dye systems and QDs as imaging agents, enabling effective imaging of numerous biological systems, with minimal toxicity.[16-18] However, CPNs have also been utilized as agents in PDT and photothermal therapy (PTT)[15,19] and, while in many such cases the PDT/PTT properties are endued through the addition of dopants,[20-22] examples exist where such the PDT/PTT properties stem from the CPNs themselves.[21] Thus, the idea of CPNs as "safe" and "non-toxic" imaging agents can be at odds with their photo-toxicity as PDT/PTT agents. However, this paradox also offers an opportunity to exploit CPNs for theranostic applications, combining their NIR imaging and photosensitization abilities for simultaneous detection and treatment of cancer.

PTB7 (Poly({4,8-bis[(2-ethylhexyl)oxy]benzo[1,2-b:4,5-b′]dithiophene-2,6-diyl}{3-fluoro-2-[(2-ethylhexyl)carbonyl]thieno[3,4-b]thiophenediyl})), whose structure is shown in Figure 1(b), is a standard conjugated polymer that has received much attention for solar energy devices because of its low bandgap, with related absorption and emission in the NIR spectral region.[23]

However, it is known to produce ROS under photoexcitation, requiring mitigation strategies when it is utilized in solar energy devices, as it leads to degradation of thin films.[24] However, for theranostic purposes, its optical and photosensitization properties offer great advantages. Hereby, we report the development of three NIR-fluorescent CPN probes based on PTB7, which are capable of photosensitization of ROS upon excitation in the first biological window (NIR-I). This establishes them as a promising nanomaterial system for PDT-based theranostic applications.

RESULTS AND DISCUSSION

Fabrication and initial characterisation of conjugated polymer nanoparticles.

Bare PTB7 CPNs were prepared using the re-precipitation method[25] (see Methods section), which is extremely facile, reliable and does not require the use of any additives or surfactants which need to be removed at the end, making it an easily scalable process. Furthermore, the reprecipitation method directly produces an aqueous dispersion of the CPNs, which is ideal for biological applications. Briefly (Figure 1(a)), the PTB7 conjugated polymer was first dissolved in tetrahydrofuran (THF), in which it has good solubility, and then injected rapidly into water, in which it has poor solubility, under sonication and vigorous stirring. It should be noted that most samples of bare PTB7 CPNs produced in this manner were unstable in aqueous solutions, precipitating within hours. This, however, could be easily overcome through the addition of an amphiphilic co-polymer to the PTB7/THF solution, prior to injection into water. Upon injection, the rapid exposure to water drives the amphiphilic co-polymer into a micelle, with the hydrophilic blocks exposed to the aqueous environment, while the hydrophobic blocks flare into the PTB7-containing core.[26]

F127 and PSMA, whose chemical structures are shown in Figure 1(b), are two co-polymers often employed for such purposes and were used here to improve the solubility of our PTB7

CPNs in aqueous environments. To enable direct comparison of different CPNs and to minimize any changes of CPN properties arising as a result of different synthesis conditions, same PTB7 polymer/copolymer ratios were used to prepare F127 and PSMA coated CPNs.

PTB7 CPNs coated with F127 and PSMA, herein referred to as PTB7@F127 and PTB7@PSMA CPNs, had significantly improved stabilities in aqueous solutions, remaining stable as suspensions for more than 6 months (see SI for full discussion of sample stabilities under different conditions). The improved stability also allowed us to employ centrifugal ultrafiltration as means of concentrating these CPN samples. Samples of high concentration are of great value to bio-applications, because it reduces the amount of solvent that is introduced into the bio-system, which can have a negative impact.

Briefly, the sample was placed on a membrane whose pore size (30kDa) was large enough to pass individual strands of F127 (12.6 kDa) but too small to allow CPN particles through it. The sample was then centrifuged, which drew the solvent together with individual copolymer strands through the pores under the influence of the centrifugal force. In such a way, and up to a certain extent, the sample above the membrane was gradually concentrated. We note that there existed an optimum combination of centrifugation speed and duration that produced the highest possible concentration of well-dispersed samples without a significant reduction in the yield of the preparation process (over-centrifugation of the sample caused the sample to adhere to the ultrafiltration membrane to an extent where it was no longer dispersible). In our case, the highest concentrations obtained for the coated samples was 420 µg/mL, whereas the highest concentration attained for the bare PTB7 CPNs was 90 µg/mL. Even at the highest concentrations, the CPN-containing dispersions were homogenous and clear, with no observable aggregates.
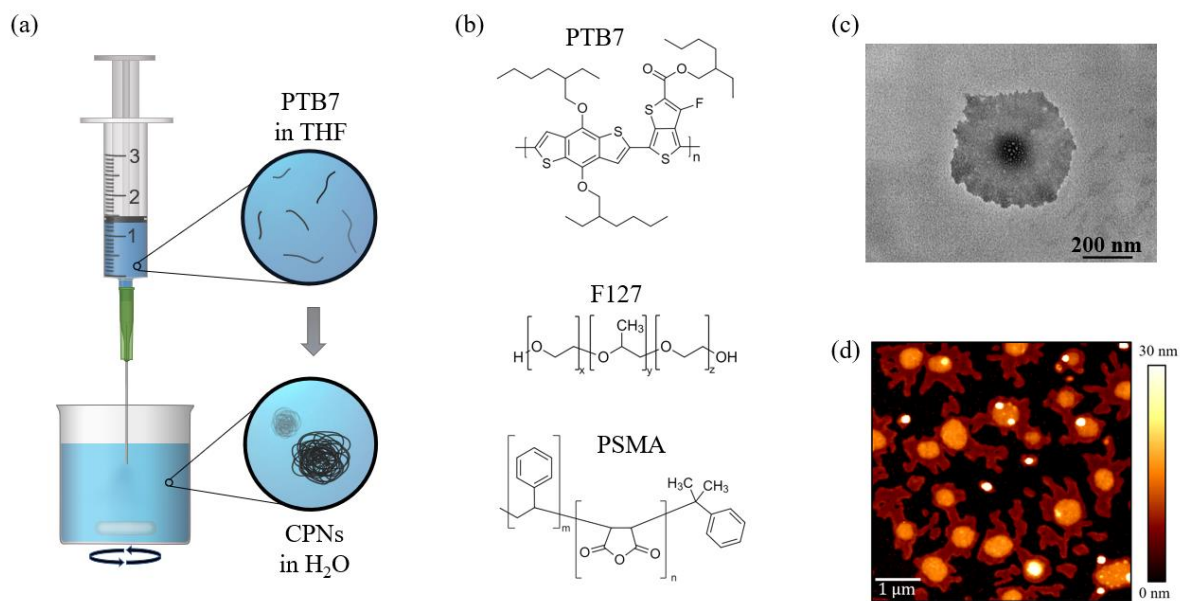
Figure 1. Fabrication of PTB7 CPNs using the nanoprecipitation method. Panel (a) summarizes the process used to prepare the nanoparticles of PTB7 conjugated polymer. To prepare coated PTB7 CPNs, Pluronic F127 or PSMA were added to the PTB7 solution in THF, prior to injection into water. Panel (b) shows the chemical structures of PTB7, F127 and PSMA. Panels (c) and (d) show TEM and AFM images of PTB7@F127 CPNs dried on appropriated substrates, respectively. The process of drying the CPNs on a substrate results in flatter, larger-diameter particles, so the sizes apparent in the TEM and AFM images exceed those determined from DLS.

The hydrodynamic size of the as-prepared and filtered CPNs was measured using dynamic light scattering (DLS). As expected, the size of the bare PTB7 CPNs was the smallest at a mean size of 140 nm, with a standard deviation of ~50 nm; the PTB7@PSMA CPNs were slightly larger at 150 ± 40 nm, while PTB7@F127 CPNs were the largest at 190 ± 60 nm (Figure 2a). The size of the coated CPN samples remained unvaried for a large range of sample concentrations (Figures 2b and S2.2 for PTB7@F127 and PTB7@PSMA data respectively)

with only a slight increase in sample polydispersity, which is a testament to their stability as colloidal dispersions.

The different sizes of the two coated CPN samples could be attributed to the different sizes of the copolymer chains ($M_n(PSMA) \approx 1900$ Da, $M_w(F127) \approx 12600$ Da). Our hypothesis is that the size of the copolymer not only directly impacts the thickness of the coat,[27] but it also plays a role in the steric effects that determine the degree of inter-collation of the copolymer chains into the PTB7 core and the packing of the PTB7 polymer chains inside the core. Thus, co-precipitation of PTB7 with the shorter PSMA co-polymer yielded CPNs that were only slightly larger than the bare PTB7 CPNs, while the presence of the longer F127 copolymer during the co-precipitation process leads to bigger CPN sizes and a relatively loose packing of F127 copolymer in the coat (Figure S3.3). The latter fact was evidenced by the much larger size and polydispersity of the as-prepared PTB7@F127 CPN samples (220 ± 60 nm), compared to those that were filtered (see middle graph of Figure 2(a)). The centrifugal ultrafiltration process removed the loosely bound F127 from the surface of the CPNs, resulting in smaller CPN sizes described above. The looseness of the F127 coat was further evidenced by the atomic-force microscopy images of the dried PTB7@F127 samples: in Figure 1(d), it is clear that the PTB7 core remains relatively intact upon drying, while the F127 coating layer is more fluid and spreads out around each CPN during the drying process (see SI for a further discussion of F127 coat fluidity).
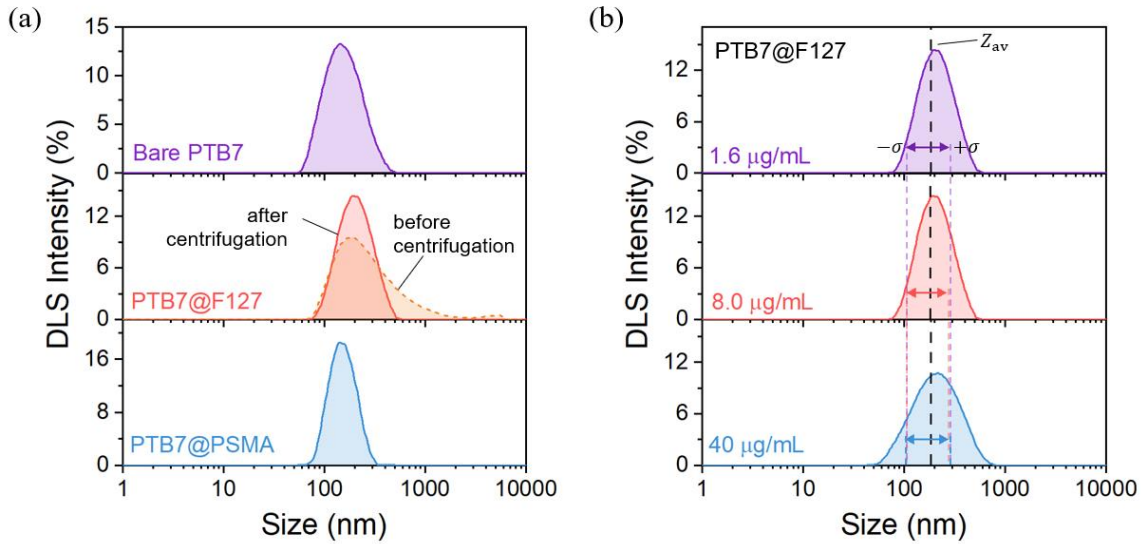
Figure 2. Hydrodynamic sizes of PTB7 CPNs. Results of DLS measurements of aqueous dispersions of (a) different PTB7 CPNs and (b) different concentrations of PTB7@F127 CPNs. In panel (a), the size of PTB7@F127 CPNs was measured before (dashed orange line) and after (solid red line) centrifugal ultrafiltration. In panel (b), the dashed black line indicates the average size (Z_{av}) of the CPNs across the three samples and the arrows indicate the range of size falling with a single standard deviation σ. Corresponding colored dashed lines run vertically across the panel for easier comparisons of the samples.

Both transmission electron microscopy (TEM) and atomic force microscopy (AFM) images (Figures 1(c) and (d) respectively) confirmed the expected core-shell structure of the CPNs co-precipitated with a copolymer. However, the heights and widths of the CPNs obtained from these images did not match those measured by DLS, yielding much larger widths (400-1000 nm) and smaller heights (10-30 nm). We attribute this to the capillary and centrifugal forces that the CPNs experience during the spin-coating and drying process, which deform them into "fried egg"-like shapes and yields the observed deviations in measured widths and heights. This hypothesis is supported by an observation that the mean volume of spherical CPNs, calculated using their average hydrodynamic diameter, $V_{\text{DLS}} \approx 3.1 \times 10^{-3}$ fL , is

approximately same as the mean obtained from the AFM data, $V_{\text{AFM}} \approx 4.7 \times 10^{-3} \text{ fL}$, especially in view of possible deformation of particles under the forces they experience during sample preparation. Further details of these calculations can be found in the supporting information (SI) document.

The sizes of the CPN particles produced in this work sit within the range identified by several studies as being optimum for accumulation in tumorous tissues (*in vivo*) by the enhanced permeability and retention effect.[28–30] Further specificity to tumorous tissues could be achieved relatively easily by modifying the re-precipitation mixture to include a copolymer coating material that has been pre-functionalized with targeting entities, or with functional groups that could be used for attachment of such entities post-reprecipitation of the CPNs. In a similar way, other modalities could also be endued onto the CPNs, while maintaining their native theranostic capability arising from the PTB7 core.

Optical properties of PTB7 CPNs

The absorption spectra of all PTB7 CPNs (Figures 3a and S4.4a) showed the characteristic two-peak absorption in the 550-750 nm region, with absorption maxima at approximately 615 nm and 675 nm corresponding to the transitions between the ground state and the first two vibronic levels of the excited state of PTB7.[31] Deconvolution of these spectra into contributions corresponding to these two transitions (see SI document) showed that the two absorption peaks were slightly blue-shifted for the bare PTB7 CPNs compared to the coated samples, which we attribute to a shorter characteristic length of the conjugated segments in bare PTB7 CPNs originating from an increased contortion of the chains in these particles. Furthermore, the relative intensity of the two absorption peaks was much smaller for these CPNs, when compared to coated CPNs and the free PTB7 chains dissolved in THF (Table S4.1). The ratio of the peaks or, equivalently, the intensity of the lower-energy peak (at 675 nm) is known to

be sensitive to aggregation in PTB7 chains, with increased inter-chain interactions causing a decrease in its intensity;[31,32] therefore, the observed decrease can be attributed to decreased inter-chain interactions. Most likely, this is due to an increased chain disorder which disturbed the $\pi - \pi$ stacking of the conjugated domains and therefore caused a reduction in interchain interactions.[31] In the coated samples, the presence of copolymers mitigated some of the steric hindrance owing to the bulky side chains of the PTB7, and allowed for tighter and better-ordered packing of the PTB7 chains; this promoted inter- and intra-chain interactions and resulted in increased absorption by excitation into the lowest vibronic excited state.
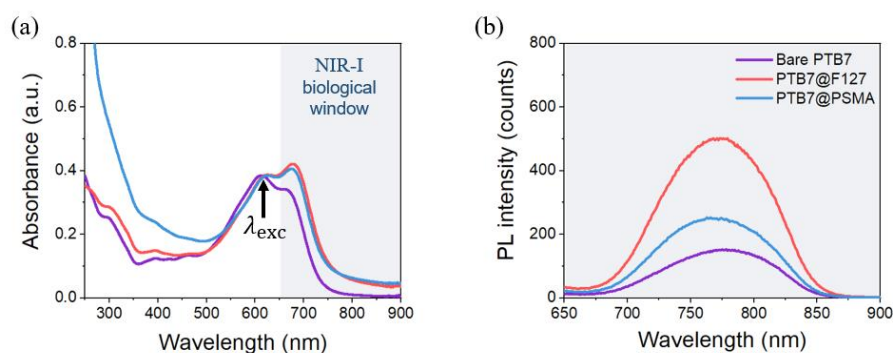

Figure 3. Optical properties of PTB7-based CPNs in aqueous solutions. Steady-state (a) absorption and (b) emission spectra of PTB7 (purple), PTB7@F127 (red) and PTB7@PSMA (blue) CPNs. The shaded region indicates the first (NIR-I) transparency region of biological tissues. The photoluminescence spectra shown in (b) were recorded using an excitation wavelength of 618 nm, as indicated by the arrow in panel (a), where all samples absorbed equally. The concentration of all samples was ~8 µg/mL.

The photoluminescence spectrum of all three CPN samples appeared to consist of a single, approximately gaussian, peak in the 700-850 nm spectral region (Figure 3(b)). The average position of the fluorescence peaks (~1.55 eV) and the corresponding Stokes' shifts (~100 nm)

were consistent with previously reported results for PTB7 films and solutions,[31,33] which attributed this peak to a de-excitation *via* emission from a lowest vibrational level of the excited state to the 1st vibrational level of the ground state. No emission corresponding to the de-excitation into the 0th vibrational level (expected to appear at ~1.86 eV) was observed in our case, indicating that most of the observed emission is from densely-packed and weakly-interacting H- aggregates.[32]

A further careful examination of the PL spectra led to the conclusion that each PL peak consisted of two Gaussian contributions (Figure S4.7, Table S4.2), located at approximately 1.55 and 1.65 eV for all samples; the observed red- and blue-shifts between different samples were solely the result of different ratios of these contributions (Figure S4.7, Table S4.2). We note that the separation of these contributions (~0.1 eV) was half of the typically-reported vibronic splitting of the ground state (~0.2 eV), both for PTB7 solutions and thin films.[31] In addition, in H-aggregated emission, de-excitation to the 0th vibrational level is forbidden and is typically not observed unless a high degree of disorder is present, *e.g.* in dilute PTB7 solutions where interchain interactions are minimized.[32] As above discussion indicates, this exception does not apply to our densely packed nanoparticles of PTB7. Therefore, it is unlikely that the origin of dual-contribution emission has to do with the vibronic splitting of the ground state. Instead, we suspect that they correspond to emissions from two different excited state species or the existence of two "populations" of conjugation lengths in our CPNs. Further investigations are underway to elucidate the exact nature of the observations.

The PTB7@F127 CPNs had the strongest fluorescence; its fluorescence quantum yield (QY) was measured to be 1.3% using the relative method[34] with Atto700 dye used as a reference (see SI for details). The QYs of the bare PTB7 CPNs and PTB7@PSMA CPNs (0.5% and 1.0% respectively) were determined relative to PTB7@F127 CPNs (see SI for details). These values were of the same order of magnitude as the QY of the PTB7 polymer in solid films (2%)[35] and

when dissolved in THF (1.52%; see SI), indicating that the packing of the PTB7 chains into a CPNs did not have a major detrimental impact on the fluorescence properties of the PTB7 polymer. Furthermore, the increased QYs of the coated samples correlated with the improvement in the colloidal stability of these CPNs in aqueous solutions (see SI for stability discussions) and the corresponding changes of their absorption and emission spectra. Therefore, we expect this to be due to the nature of the excitonic species that are formed in the individual CPN samples, as determined by intra- and inter-chain interactions,[31] which are inevitably influenced by steric and other interactions between the chains of the PTB7 and F127/PSMA copolymers.

While the fluorescence QYs of our CPN samples were low (0.4-1.3%), in terms of their absolute values, these values are not atypical of many NIR emitters. Furthermore, even faint NIR-I fluorescence can be detected relatively efficiently because of the reduced autofluorescence contributions typically observed in this spectral range. More to the point, to function effectively as photosensitizers for PDT, our CPNs require an efficient intersystem crossing from the singlet excited state to the triplet excited state, a process which competes with direct de-excitation *via* emission and therefore necessarily favors a CPN with a low fluorescence QY. One should note, however, that the addition of the copolymer coating was shown to improve the fluorescence QY of the PTB7 CPNs, which is consistent with previous observations of coated CPNs made from different conjugated polymers.[19,36] Furthermore, this improvement did not come at the expense of an inhibition of ROS production, as discussed in the next sections.

It is important to highlight that the demonstrated optical properties of PTB7 CPNs are highly advantageous for bioimaging applications – they partially absorb and emit in the NIR spectral region, allowing *linear* excitation and collection of emission in the NIR-I biological transparency window. The large (~100 nm) Stokes' shifts between their absorption and

emission bands allow for facile and efficient implementation into off-the-shelf imaging systems, requiring nothing more than a standard continuum lamp or laser, and a judicious choice of filters. As such, the optical properties of the developed PTB7 CPNs allow facile bioimaging in the NIR-I biological transparency window, while at the same time overcoming the commonly reported drawbacks for NIR-I theranostic polymer nanoparticles, such as low photostability, rapid and irreversible photo-degradation, and poor aqueous solubility (see SI for stability evaluation of our CPNs).

Singlet oxygen production by CPNs

Singlet oxygen ($^1O_2$) is a highly energetic and reactive form of molecular oxygen that can be formed by triplet-triplet energy transfer between the triplet ground state of molecular oxygen and a triplet excited state of a photosensitizer.[37–39] The triplet excited state of PTB7 have been previously reported to be sufficiently energetic to generate singlet oxygen – in fact this process is widely acknowledged to cause degradation of thin PTB7 films.[24,40,41] However, and as suggested above, this property can be exploited for PDT applications.

Hence, the ability of our CPNs to produce singlet oxygen was evaluated using a chemical sensor – Singlet Oxygen Sensor Green – which turns from a non-fluorescent form (SOSG) into a highly fluorescent form (SOSG-EP) upon reaction with singlet oxygen (Figure 4(a)).[42] The production of singlet oxygen by the CPNs was continuously stimulated using a red CW laser (λ_{stim} = 635 nm). After every 30 seconds of stimulation, the SOSG-EP fluorescence was recorded (λ_{exc} = 500 nm). As shown in Figure 4(b), the SOSG did not absorb at the stimulation wavelength, and conversely, the CPNs do not fluoresce at wavelengths where SOSG-EP emits, thereby minimizing any crosstalk. In all cases, the concentration of the tested samples was adjusted so that they all absorbed equally at the stimulation wavelength (*i.e.* at 635 nm). Control experiments involving evaluation of absorption spectra of CPN/SOSG mixtures post-

measurements were performed to confirm photochemical and structural stability of the CPNs during these measurements (see "Photochemical stability of CPNs during singlet oxygen measurements" section in the SI document).

We note that the excitation wavelength of 635 nm was chosen because of the compatibility of the 635 nm laser diode with the integrated spectrophotometer. In principle, any excitation wavelength in the 600-750 nm spectral range could be used instead, including those in the NIR spectral region, since the SOSG does not absorb there (Figure 4(b)).
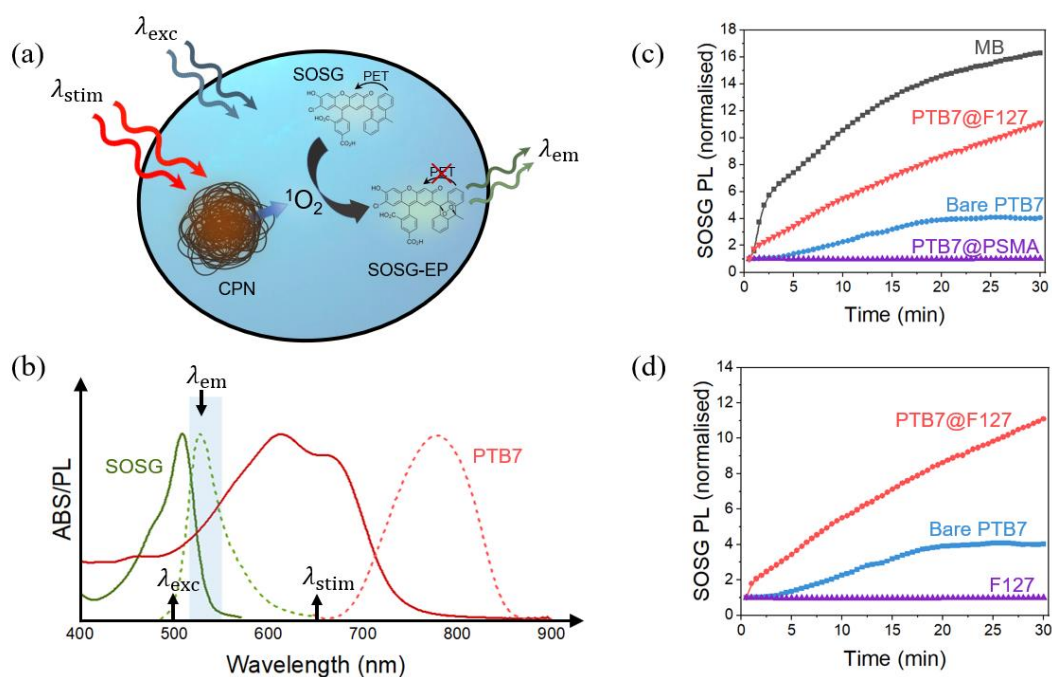

Figure 4. Measurements of singlet oxygen production by PTB7 CPNs using SOSG chemical sensor. (a) The measurement scheme consisted of continuous stimulation of singlet oxygen production by the CPNs, conversion of SOSG into its fluorescent form SOSG-EP *via* a reaction with singlet oxygen and a recording of SOSG-EP to evaluate the amount of singlet oxygen produced by the CPNs. The arrows in panel (b) indicate the relevant wavelengths used in the experiments, along with normalized absorption and emission spectra of SOSG and PTB7 CPNs. Panel (c) shows the temporal evolution of the SOSG-EP fluorescence signal for different types of CPNs and a reference photosensitizer (methylene blue, MB). Panel (d) compares

14

singlet oxygen production by the PTB7@F127 CPNs, the bare PTB7 CPNs and the F127 copolymer. For all measurements, samples had absorbances of ~0.5 at the stimulation wavelength (635 nm) prior to the addition of SOSG. This corresponded to CPN samples' concentrations of ~10 µg/mL and a concentration of 7.6 µM for MB solution.

Bare PTB7 CPNs produced singlet oxygen steadily over the 30 minutes measurement period (Figure 4(c)). Since the lifetime of the singlet oxygen in heavy water is of the order of tens of microseconds,[43,44] and the decay of SOSG-EP fluorescence occurred with a characteristic lifetime of ~18 minutes (see section 5 of SI), the observed trend represents a continuous generation of SOSG-EP throughout the measurement period. The plateau reached at approximately 20 minutes into the measurement thus represents a steady state characterized by equal rates of SOSG-EP production *via* the process described above and the decay of its fluorescence due to diffusion out of the excitation volume (see the discussion of ROS production under prolonged stimulation in SI for further information).

Interestingly, the PTB7@F127 CPNs exhibited a marked improvement in singlet oxygen production: a 2-fold improvement was observed over a 30-minutes measurement period, as shown in Figure 4(c), and a 7.5-fold improvement was achieved over a 3-hour period (data shown in Figure S5.2(c) in SI). The F127 copolymer on its own produced no singlet oxygen (Figure 4(d)) and hence was not the source of the observed increase in the SOSG-EP fluorescence signal.

Production of singlet oxygen by the PTB7@F127 CPNs was stable, with no observable decreases in the signal during stimulation periods lasting up to 3 hours (data in SI). This was contrary to our control experiments with methylene blue (MB), which exhibited a steady decrease in the SOSG-EP signal after 30 minutes of initial increase (data in SI). Most likely, this decrease can be attributed to MB undergoing gradual photodegradation during the prolonged stimulation.[45] In fact, despite the initially lower singlet oxygen yield of our

PTB7@F127 CPNs (8.5% in ethanol and 32.4% in water) compared to that of MB (52% in ethanol and 50% in water), the CPNs perform better than MB when longer exposure times are considered (see SI for further details of these measurements). This clearly demonstrates the advantage of CPNs over molecular photosensitizers for PDT applications, in which prolonged continuous exposures often result in photobleaching and an associated reduction in efficiencies.

It is important to note that the nature of the copolymer coats was critical in determining the performance of the PTB7 CPNs as singlet oxygen producers. Whilst the addition of the F127 coat resulted in a 7.5-fold improvement of the singlet oxygen production compared to bare PTB7 CPNs, the addition of PSMA coat completely quenched it! This observation cannot be explained by the different size/density/nature of the copolymer coats, all of which affect the diffusion of the molecular oxygen through the coat. This is because both F127 and PSMA are amphiphilic polymers that contain oxygen in their composition and whilst F127 does form looser shells compared to PSMA, the PSMA shells are smaller than F127; therefore we expect the diffusion of molecular oxygen to be comparable for the two. Equally, the difference in singlet oxygen production cannot be attributed to any differences of the photophysical processes occurring within the core of the CPNs, *i.e.* within the PTB7 polymer itself. The absorption, emission and excitation spectra of the two coated CPNs samples are very similar (see SI figures S4.4 and S4.5 for normalized spectra that allows easier comparison); this suggests that the key photophysical processes occurring in the PTB7 cores are identical for the two CPN types. Therefore, the observed quenching of singlet oxygen production must originate at the interface of the CPN core and its copolymer coat, with PSMA completely quenching the triplet excited state of the PTB7 and the F127 facilitating the triplet-triplet energy transfer from PTB7 to molecular oxygen.. This photo-initiated toxicity dependency on the capping agent highlights the significance of its role in determining the properties of the CPNs, and explains why some CPNs are described as non-toxic[46–48] whilst others are reported to be PDT-active.[19,49]

It is expected that further investigations into these aspects will allow on-demand modulation of phototoxic behavior of CPNs *via* an appropriate selection of its solubilizing shell.

Superoxide production by CPNs

Photodynamic therapy does not always rely on the singlet oxygen production – other ROS can also be exploited. Therefore, we also investigate the possibility that our CPNs could produce another type of ROS – the superoxide radical of oxygen, O_2^- – which is also known to cause cell damage.[50,51] In this study, O_2^- production by CPNs was measured directly and in real-time by using chronoamperometry.[52–54] This involved the use of a gold electrode to which cytochrome *c* was bound. The cytochrome *c* was reduced to its Fe^{2+} state by O_2^- produced by CPNs, before being re-oxidized to its Fe^{3+} state at the electrode surface. This redox cycling led to a current that was proportional to the rate of O_2^- production, as shown in Figure 5(a).
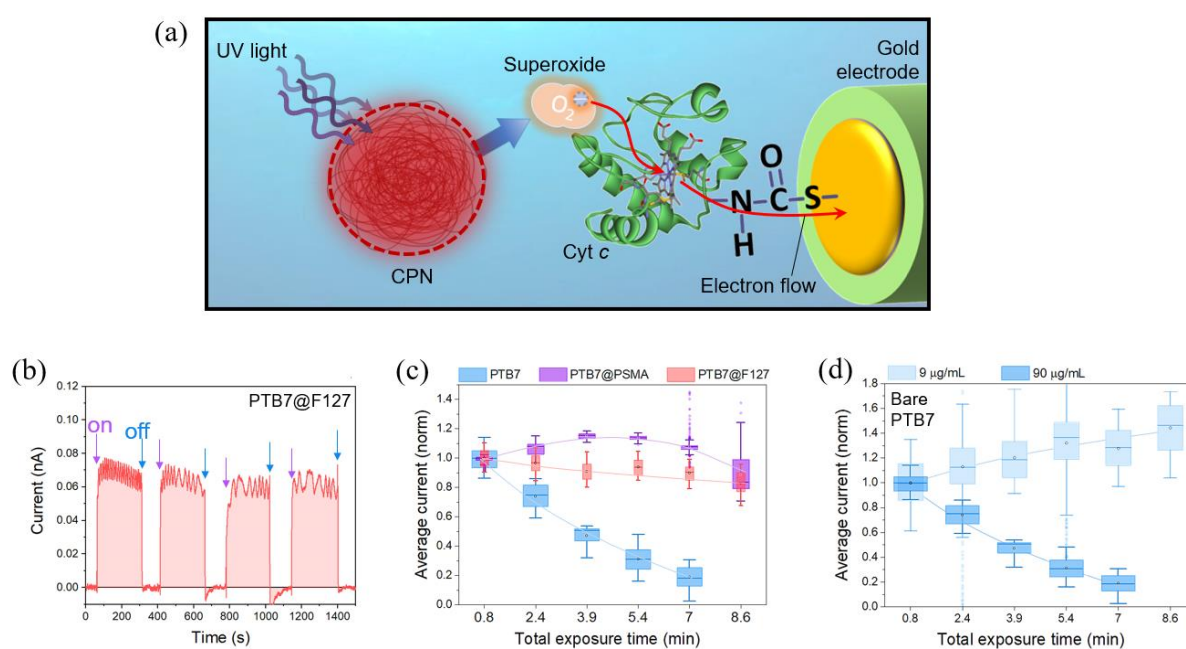

Figure 5. Superoxide production by CPNs in response to photostimulation at 365nm. (a) Schematic showing the proposed mechanism of electrochemical superoxide detection by CPNs using a cytochrome *c* functionalised gold electrode, poised at +100 mV. **(b)** Repeated photostimulation of 40 µg/mL PTB7@F127 CPN sample at 365nm produced reproducible

current spikes. **(c)** The effect of PSMA and F127 coating on superoxide production by PTB7 CPN samples of high concentrations (90 for bare PTB7 and 100 µg/mL for PTB7@PSMA and PTB7@F127 CPNs). **(d)** The effect of CPN concentration on superoxide production, demonstrated using the bare PTB7 CPN sample. Each data point in panels **(c)** and **(d)** represents an average of 80 seconds worth of data (1.2 min). During the photostimulation, the light source was consistently positioned at a distance of 10 mm away from the electrode/CPN solution.

Measurements showed that all three PTB7 CPN samples produced superoxide radicals upon illumination at 365 nm with a 6 W lamp (Figure 5). Note that the 365 nm wavelength was chosen as it contributed minimally to the measured electrical currents; conversely, the use of light sources emitting in the red or NIR spectral regions, although superior for excitation of CPNs, was impractical in this case as it caused direct photoexcitation of the gold electrode, resulting in measurements of overwhelmingly large currents that overshadowed those arising as a result of superoxide production by CPNs. Further control experiments involved using periodic illumination and addition of 100 µg/mL of superoxide specific scavenger superoxide dismutase (SOD). The modulation by periodic illumination (Figure 5(b)) and its quenching by SOD (Figure S6.1) confirmed that the current measured was superoxide radical specific and that it was, in all cases, photoinitiated (see SI for further details). Unusually, at relatively high CPN concentrations of ∼100 µg/mL, the initial rate of superoxide production was comparable for all three samples (see the non-normalized data in SI), indicating that it originates from the PTB7 core. However, on continued exposure to UV radiation (Figure 5(c)), the superoxide production by bare PTB7 CPNs decreased rapidly, indicating a potential degradation of the sample. In contrast, the coated CPN samples experienced only a moderate decrease in the superoxide production (<15%) over the ∼9 minutes irradiation period. This is significant because, at high concentrations, there is a high probability that the photo-generated superoxide

radical will encounter and cause damage to another CPN, degrading the sample, whereas lower concentration reduces this risk, as seen for bare PTB7 CPN sample of low concentration in Figure 5(d). Clearly, and importantly, the F127 and PSMA copolymer coats are sufficient to protect the PTB7 core from unfavorable photodegradation even at high sample concentrations, which maintains their ability to produce ROS such as superoxide radicals for longer periods of time. The protection offered by the copolymer coats against the ROS produced by the CPNs themselves, and the consequent longevity of the sample, is critical for the implementation of PTB7 CPNs as PDT-enabled probes *in vivo*.

In vitro ROS production by PTB7 CPNs

The optical, physical, and photochemical properties of our CPNs in aqueous dispersions, as described above, clearly demonstrate their potential as photosensitizers. To determine whether they would perform equally well in more complex, biologically relevant environments, we tested their feasibility as PDT agents by performing an intracellular ROS assay (see Methods for details).

The HaCaT cell line (immortalized human keratinocyte skin cells) was chosen for the purpose because PDT is particularly suited to the treatment of skin conditions. The full experimental details of the intracellular assay can be found in the Methods section. Briefly, the assay involved the use of a non-fluorescent sensor 2',7'–dichlorofluorescin diacetate (DCFDA) which is oxidised into a fluorescent form 2',7'–dichlorofluorescein (DCF) by hydroxyl, peroxyl and other ROS. In this case, the ROS were produced by the CPNs following irradiations with a lamp whose emission spectrum covered the first biological transparency window (660-850 nm). The resulting fluorescence signals from DCF yielded a measure of ROS production by the CPNs, measured in % relative to tert-butyl hyperoxide (TBHP, positive control, 100% ROS production), and the medium only as a negative control (0% ROS

production). As non-irradiated controls, cells dosed with the same concentrations were incubated under light exclusions for the same durations as the irradiation course, to ensure the same exposure conditions.
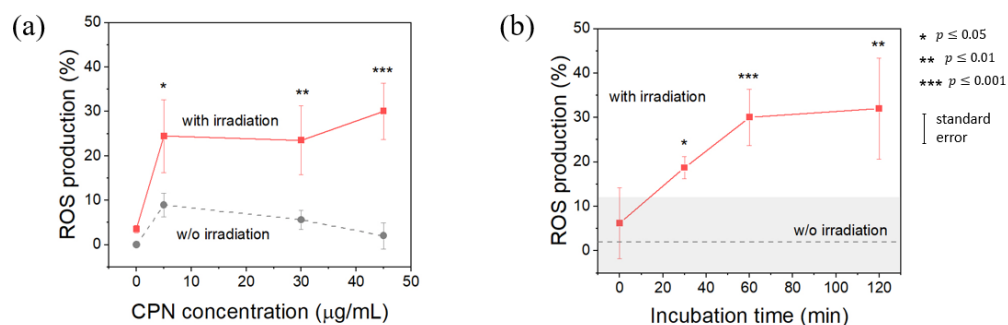

Figure 6. *In vitro* **ROS production by PTB7 CPNs** in HaCaT cells incubated with PTB7@F127 CPN samples at concentrations up to 45 µg/mL (a). Cells were incubated with (red data points) and without NIR irradiation (grey data points) for 60 minutes prior to ROS measurement. The intracellular ROS production was also measured as a function of time following exposure to 45 µg/mL PTB7c@F127 CPNs (b). The dashed grey line and the height of the light grey box correspond respectively to the mean and standard deviation of ROS production for non-irradiated cells exposed to 45 µg/mL CPN samples. Each data point is an average of three repeats ($n = 3$). For all measurements, the NIR source used for irradiation of samples had a broad emission profile covering the 660 – 850 nm spectral range.

Results of the assay showed that non-irradiated samples incubated with CPNs produced relatively small amount of ROS, and the differences in DCF signal of these samples and the negative control were not statistically significant ($p > 0.05$; Figure 6 and Figure S8.1). The presence of CPNs had minimal detrimental effect on cell proliferation; this fact was confirmed by a viability assay, as discussed in Section 8 of the SI. Irradiated samples, however, showed a significant and dose-dependent increase in ROS production ($0.001 < p < 0.05$, as indicated by asterisks in Figure 6). Furthermore, for the highest concentration (45 µg/mL), there was a

statistically distinguishable increase of DCF signal for incubation times of up to 60 minutes ($p < 0.05$ between 0/30 min and 30/60 min timepoints), after which the signal did not vary significantly ($p > 0.05$ for 60/120 min). These results confirm the ability of our CPNs to generate ROS under photoexcitation in biological environments and validate their photosensitizing abilities under NIR-I excitation.

PTB7 CPNs as NIR-I imaging agents

The existence of other modalities besides photosensitization, such as those allowing *in situ* imaging of tissues, are of particular interest for theranostic applications of nanoparticle-based agents because they allow delineation of treatment areas and therefore constitute a non-invasive diagnostic tool. In many cases, imaging modalities are achieved through addition of a dopant (*e.g.* covalent conjugation of an MRI probe to the nanoparticle surface). However, PTB7 CPNs are inherently NIR fluorescent, thereby offering an in-built imaging modality. To demonstrate the potential of PTB7 CPNs for theranostic applications, we imaged the NIR fluorescence of our CPNs in A549 cell cultures . The uptake was assessed semi-quantitatively based on the evaluation of the fraction of cells showing both internalization and stable external adherence after multiple washes. The experimental details are provided in the Methods section.

The recorded images confirmed that the CPNs were widely but non-uniformly distributed within the cells (Figure 7 and Figure S7.1 in SI). Samples incubated with the bare PTB7 CPNs, showed the weakest fluorescence signals (Figure S7.2), consistent with the lowest fluorescence QY of this sample. Of the two coated samples, PTB7@PSMA CPNs provided the strongest fluorescence signals, evaluated in terms of the photons recorded per pixel of NIR fluorescence image, despite having a lower fluorescence QY than PTB7@F127 CPNs (Figure S7.2); we attribute this to a more efficient internalization of the PTB7@PSMA CPNs by the A549 cells and note that a different trend could be observed for other cell lines.
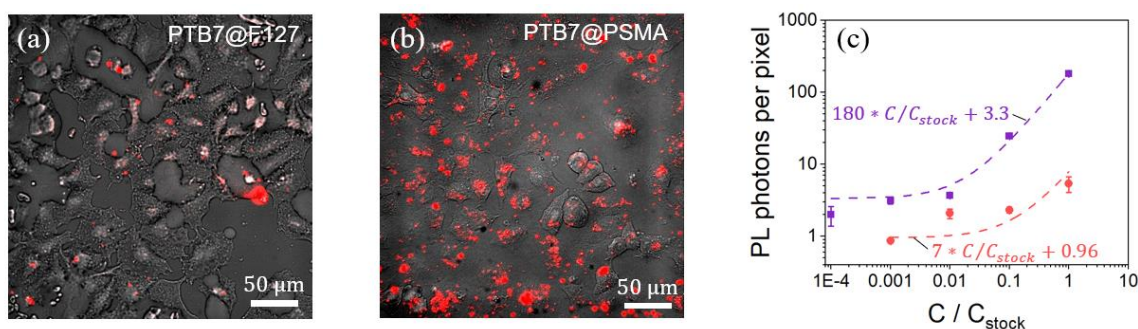
Figure 7. PTB7 CPNs as *in vitro* NIR fluorescence imaging probes. Human lung epithelial cells (A549) following incubation with **(a)** PTB7@F127 and **(b)** PTB7@PSMA CPNs at concentration $C_{stock} = 150\ \mu g/mL$, imaged using 40x objective and RG715 filter (700-1000 nm). In both panels, the NIR fluorescent image (red) under 400-650 nm excitation is superimposed on (greyscale) ambient-light image. **(c)** The number of detected fluorescence photons (average per pixel) arising from PTB7@PSMA (purple data) and PTB7@F127 CPNs (red data) imaged through 10x objective, for different concentrations. Error bars are standard errors, based on measurements in eight subregions of recorded image. The linear fit to the data (dashed lines) were obtained using OriginLab 2019b software and are shown as guidelines only.

Fluorescence images of cells incubated at lower concentrations of CPNs suggested a concentration-dependent nanoparticle uptake and fluorescence: for coated PTB7 CPNs, the average number of fluorescence photons scaled linearly with CPN concentration during incubation, as expected (Figure 7(c)). Ambient images of these samples confirmed that neither the reduced fluorescence signals for different capping agents (Figure 7(b)) nor lower CPN concentrations (Figure 7(c)) are due to variations of cell numbers and distributions, which were similar in all cases (Figure S7.3).

Therefore, the improvement of the fluorescence signals for PTB7@PSMA CPNs is again attributed to the higher affinity of PSMA to A549 cells, resulting in larger overall CPN numbers being retained on the sample post-incubation and washing (Figure 7). This agrees with existing

literature on PSMA, in that it is known to facilitate the penetration of the lipid bilayer of cell membranes, and the internalization and binding of drug-polymer conjugates with the hydrophobic milieu of the cell.[55–57] PTB7@F127 CPNs, on the other hand, demonstrated reduced cell uptake and internalization into the A549 cells, as is expected for folate receptor-deficient cells.[58] We note, however, that this folate receptor-dependent uptake of the PTB7@F127 CPNs, along with well-established functionalization of these CPNs with appropriate ligands,[59,60] can be exploited to achieve tumor type-specific uptake[61,62] and therefore a high degree of selectivity to tumorous tissues in theranostic applications. Nonetheless, these results perfectly demonstrate that the capping copolymers are crucial in determining the particle uptake profiles; therefore, a promising future direction is the control of CPN functionalization aimed at ligand-mediated targeting.

CONCLUSION

In this work, we have successfully prepared PTB7 CPNs, both bare and coated with F127 and PSMA copolymers. We demonstrated that the prepared CPNs have many advantageous properties for theranostic applications that consolidate bioimaging-based diagnostics and photodynamic therapy. The optical properties of PTB7 CPNs allow linear excitation and collection of emission in the NIR-I transparency window, making them a very good bioimaging agent; their sizes are optimum for accumulation in tumorous tissues *via* the EPR effect; and finally, they generate various ROS species upon photoexcitation, including singlet oxygen with quantum yields of up to 33% in water, highlighting their potential for PDT applications.

Furthermore, we demonstrated that selection of the capping material is crucial in determining the key properties of the CPNs. These not only include their fluorescence QY, their hydrodynamic size, and their cellular uptake, but also the nature and efficiency of

ROS production. We show that, despite having similar optical and physical properties, and thus also similar chain packing and photophysics, the photosensitizing behavior of the F127- and PSMA-coated PTB7 CPNs was widely different: coating PTB7 CPNs with F127 copolymer lead to an improvement of singlet oxygen production, whilst a similar process with the PSMA copolymer led to its complete quenching.

These results highlight the critical importance of the interplay between conjugated polymer and its capping agent, and the resulting photophysical and chemical properties of the conjugated polymer nanoparticles. They also explain why most conjugated polymer particles are biologically inert yet some can display photo-initiated toxicities that can be exploited for photodynamic therapy applications.

METHODS

Material. Poly({4,8-bis[(2-ethylhexyl)oxy]benzo[1,2-b:4,5-b′]dithiophene-2,6-diyl}{3-fluoro-2-[(2-ethylhexyl)carbonyl]thieno[3,4-b]thiophenediyl}) (PTB7), Pluronic F-127 (F127), Poly[styrene-co-maleic anhydride] (PSMA), Tetrahydrofuran (THF), Methylene Blue (MB), Atto700 dye and Cytochrome c (from horses heart) were all purchased from Sigma-Aldrich. Singlet Oxygen Sensor Green (SOSG), Deuterium oxide (D$_2$O), 3,3'-dithiobis(sulfosuccinimidyl propionate)) (DTSSP) and Tris Buffer were obtained from Thermo Fisher Scientifc.

Preparation of PTB7 CPNs. To prepare PTB7 CPNs using the nanoprecipitation method described previously by Wu *et al.*, PTB7 powder was dissolved in THF at a concentration of 1 mg/mL, while the F127 (or PSMA) powder was dissolved in THF at a concentration of 100 mg/mL. The two solutions were sonicated until the powders were fully dissolved and then mixed in 1:1 ratio. 2 mL of this mixed solution were then added in step-wise manner to 10 mL of deionised (DI) water, 200 µL at a time, under ultrasonication and

vigorous stirring. The solution was then left to continuously stir for additional 72 hours in order to completely remove THF from CPNs *via* evaporation. Upon completion of this period, the sample was purified of any unbound or loosely bound copolymer by centrifugal ultrafiltration through a Millipore centrifugal filter (30 kDa, Sigma Aldrich) at 7000 rpm for 20 minutes, repeated twice.

To prepare the bare PTB7 CPNs, the protocol was essentially same, with the exclusion of addition of the F127/PSMA solution to the PTB7 solution, and a reversal of the roles of the water and PTB7 solution, *i.e.* instead of adding PTB7 to DI water, 10 mL of DI water were added to 1 mL of 1 mg/mL PTB7 solution in THF, in steps of 100 µL, under ultrasonication. The rest of the protocol remained the same.

Characterisation of CPNs. Hydrodynamic diameters of CPNs in aqueous solutions were obtained using Malvern Zetasizer Nano ZS. Atomic force microscopy images were obtained using the Bruker Icon Dimension Atomic Force Microscope. TEM imaging was performed on a JEOL 1400 Transmission electron microscope, operated at 120 kV. UV-vis spectra were recorded using a Shimadzu UV-2600 spectrophotometer. Steady-state photoluminescence spectra were recorded using an Agilent Cary 60 spectrophotometer. Concentration of samples, sizes of excitation and emission slits and integration times were adjusted as necessary to obtain a reasonable signal. Full experimental protocols for all measurements can be found in SI.

Singlet oxygen generation. Production of singlet oxygen by CPNs in aqueous solutions was monitored using a spectroscopic method, employing the Singlet Oxygen Sensor Green (SOSG) as a chemical sensor, according to the manufacturer's instructions. The test solution was prepared by diluting 100 µL of 100 µg/mL CPN solution in 400 µL of TRIS buffer and 500 µL of D_2O, in a 1400 µL microcuvette (Hellma). For comparison measurements, the concentration of the samples was further and finely adjusted by addition of minute amounts of D_2O, to ensure

same absorbance by all samples at the stimulation wavelength (635 nm). To this, 0.2 µL of 5 mM SOSG probe was added in the dark just prior to the start of spectroscopic measurements. Singlet oxygen production by the CPNs was continuously stimulated using a 635 nm diode laser (ThorLabs, 4.5 mW) with an elliptical beam profile (4.5 mm x 1 mm), and SOSG fluorescence at 530 nm (λ_{exc} = 500 nm) was recorded at 30 second intervals, with each spectrum recorded over a 3 second period. Methylene blue (MB) was used as a positive control, employing the same protocol as above, but replacing the CPN solution with 100 nM solution of MB instead.

The QY of singlet oxygen production by CPNs was measured using MB as a reference (Φ_{ref} = 0.52 in ethanol). Singlet oxygen production by MB was first recorded 5 min after the addition of the SOSG probe, for different concentrations of MB. These data were then used as a calibration curve to convert the SOSG fluorescence into yield of singlet oxygen for similar measurements involving a concentration series of CPN samples (full details in SI).

Superoxide radical detection. Superoxide radicals photo-generated by the CPNs were detected using chronoamperometry. A MultiPalmSense4 low-noise potentiostat (Alvatek, Gloucestershire, UK) was used for the purpose, with Ag/AgCl glass reference electrode (Clark Electrochemical Instruments Ltd, Reading, UK) and a 2 mm O.D. gold working electrode, encased in KEL-F plastic (Biotech Instruments Ltd., Kimpton, UK). Immediately prior to measurements, the working electrode was functionalised with cytochrome *c* using a protocol described previously by P. Manning *et al.*,[52] without modification. For measurements, the CPN stock solutions were diluted to the required concentrations with PBS. The working electrode was placed inside the solution and the UV lamp was positioned in such a way as to illuminate the solution from the side. Currents were then recorded for a period of up to 30 minutes, with the potentiostat operating at +100mV *versus* Ag/AgCl.

Cell culture. A549 human lung epithelial and HaCaT human keratinocyte cell lines (European cell culture collection – ECACC, and U. Nottingham respectively) were maintained in Roswell Park Memorial Institute RPMI-1649 with 10% v/v Fetal Bovine Serum (FBS) and supplemented with 100 IU/ml penicillin-100 μg/ml streptomycin solution and 2 mM L-glutamine (Sigma Aldrich, Dorset, UK). For experiments, 100 μl cells at an optimal density of 5×10^5 cells/ml (HaCaT) or 5×10^4 cells/ml in complete cell culture medium were seeded onto bottom μclear black 96-well plates (Greiner Bio-One, Gloucester, UK) and incubated overnight.

ROS and viability assays with PTB7 CPNs. The DCFDA cellular ROS detection kit (Abcam, Cambridge, UK) was used to determine the ROS production induced by photoexcitation of CPNs, according to the manufacturer's instructions. Briefly, the cells were washed with 100 μl of 1X ROS assay buffer. The buffer was then replaced by 100 μl of DCFDA solution and incubated for 45 minutes in the dark, and then replaced by PTB7@F127 CPNs dilutions in RPMI medium (0-45 μg/mL). Without allowing time for internalisation, NIR irradiation was applied with a light dose of 10 J/cm^2 at 660 - 850 nm using Derma Red Lamp (Care Lamps, Care Lamps, UK) to excite the nanoparticles. Normalised fluorescence readings from the ROS-signalling DCF with an emission wavelength of 520-530 nm were taken at time intervals of 0, 30, 60 and 120 minutes upon incubation. Positive control wells for the ROS assay were supplemented with 100μL THBP and negative control wells contained untreated cells (n=3). The result shows a significant increase in ROS production in the presence of even a very small amount of PTB7@F127 CPNs, while at higher CPN concentrations, the ROS production inevitably becomes dependent on the incubation time.

To better understand the cytotoxicity of PTB7@F127 CPNs, different concentration of PTB7@F127 CPNs with different incubation times from 0-120 min were investigated. We used the PrestoBlue (PB) assay (Life Technologies, Carlsbad, USA), a commercially available, ready-to-use, water-soluble preparation. A HaCaT viability assay with PB reagent was performed according to the manufacturer's protocol. Briefly, HaCaT cells were seeded in 96-well plate at a density of 1×10^4 cells per well. Prior to the assay, the growth medium was replaced by PTB7@F127 CPNs dilutions in RPMI (Sigma-Aldrich, USA), 0-45 µg/mL. At the end of treatment, the cells were washed with PBS and incubated with PB reagent. The viability signalling PB (resorufin) fluorescence was read (Ex/Em 560 nm/590 nm) after 0, 60 and 120 minutes. The cell viability was expressed as a percentage relative to the untreated cells.

Near-infrared imaging. Cell cultures were prepared with CPN concentrations 1/10, 1/100 and 1/1000 of the stock solutions (90 µg/mL for bare PTB7 CPNs; 150 µg/mL for PTB7@PSMA CPNs and 200 µg/mL for PTB7@F127 CPNs), by first replacing the A549 growth medium with CPN dilutions in complete culture cell medium (10 µL), and then incubating with cells for 7 hours. Following incubation, cells were washed with warm phosphate-buffered saline (pH 7.0) and fixed with paraformaldehyde. Culture-containing plates were then imaged using an Olympus IX71 fluorescence microscope in transmission mode, imaging onto a 512x512 Hamamatsu 9100-23B electron-multiplying (EM-)CCD. All images were taken through a 3 mm Schott RG715 long-pass filter (715FCS; Knight Optical, Maidstone) which, together with the EM-CCD quantum efficiency, isolated the detection sensitivity to ~700-1000 nm. Ambient and fluorescent images were obtained by varying the illumination spectrum from a 6 V, 30 W halogen lamp which provides broadband illumination; ambient images utilised , a 3 mm Schott RG665 long-pass filter (665FCS; Knight Optical), while fluorescent images were obtained through a 3 mm Schott BG39 short-pass filter paired

with a 1 mm IR-cut short-pass filter (575FCS and 400FIC; Knight Optical) restricting the excitation wavelength range to ~400-650 nm, crucially outside the ~700-1000 nm bandpass of the imaging system. Fluorescent images required moderate EM sensitivity gain. (Note that the "ambient" illumination overlaps with the CPN excitation spectrum (Fig. 3a) in the range ~650-750 nm, but ambient images are used for orientation purposes only and are in any case dominated by the illumination spectrum.) The recorded raw images were minimally processed using ImageJ (Rasband 1997).

ASSOCIATED CONTENT

Supporting Information

The following supporting information is available online: stabilities of bare and coated PTB7 CPNs under different ambient and physiological conditions; experimental details of size-characterization of PTB7 CPNs; discussion of F127 shell fluidity; calculation and comparison of PTB7 CPN volumes obtained from DLS and AFM data; experimental details of optical characterization of CPN samples; normalized optical spectra of all samples and their deconvolution into Gaussian components; further experimental details of measurements of singlet oxygen production by PTB7@F127 CPNs and related additional data; additional data for superoxide production by CPNs; additional data highlighting potential of PTB7 CPNs as NIR-I imaging agents; experimental details and additional data regrading *in vitro* ROS production by PTB7 CPNs.

AUTHOR INFORMATION

Corresponding Authors

Aliaksandra Rakovich – *Physics Department, King's College London, Strand, London, WC2R 2LS, UK；Email: aliaksandra.rakovic@kcl.ac.uk*.

Mark A. Green – *Physics Department, King's College London, Strand, London, WC2R 2LS, UK；Email: mark.a.green@kcl.ac.uk*.

Authors

Miao Zhao – *Physics Department, King's College London, Strand, London, WC2R 2LS, UK.*

Edward Leggett – *Physics Department, King's College London, Strand, London, WC2R 2LS, UK. Current affiliation: University of Oxford, Engineering Science, Begbroke Science Park, Sandy Lane, Oxford, OX1 2JD, UK.*

Struan Bourke – *Physics Department, King's College London, Strand, London, WC2R 2LS, UK. Current affiliation: University of California San Francisco, Pharmaceutical Chemistry, San Francisco, CA, USA 94143.*

Souzana Poursanidou – *Department of Clinical, Pharmaceutical and Biological Sciences, University of Hertfordshire, College Lane, Hatfield AL10 9AB, UK*

Sadie Carter-Searjeant – *Physics Department, King's College London, Strand, London, WC2R 2LS, UK.*

Steve Po – *Physics Department, King's College London, Strand, London, WC2R 2LS, UK.*

Marciano Palma do Carmo – *Physics Department, King's College London, Strand, London, WC2R 2LS, UK.*

Lea Ann Dailey – *Department of Pharmaceutical Technology and Biopharmacy, University of Vienna, 1090 Vienna, Austria.*

Philip Manning – *Translational and Clinical Research Institute, Faculty of Medical Sciences, Newcastle University, Newcastle upon Tyne, NE2 4HH, UK.*

Sean G. Ryan – *Department of Physics, Astronomy and Mathematics, University of Hertfordshire, College Lane, Hatfield, AL10 9AB, UK; Centre for Advanced Biomedical Imaging, UCL, Gower Street, London.*

Laura Urbano – *Department of Clinical, Pharmaceutical and Biological Sciences, University of Hertfordshire, College Lane, Hatfield AL10 9AB, UK.*

Author contributions

MZ contributed to all experimental work, with the exception of NIR imaging and intracellular ROS production measurements. EL and SB contributed to CPN fabrication. SC-S and SP assisted with CPN characterization (TEM and AFM). SP and LU performed the intracellular ROS production measurements. LU and SGR performed the NIR imaging of cell lines incubated with CPNs. AR and PM performed the superoxide measurements. MZ, MPC, SP, LU and AR performed data analysis. All authors contributed towards the writing of the manuscript. LAD, MG and AR are responsible for conception of the project, its direction and management of the team. All authors have approved the submitted version and have agreed to be personally accountable for their own contributions.

ACKNOWLEDGEMENTS

COMPETING INTERESTS

There are no conflicts or competing interests to declare.

REFERENCES

(1)   Dolmans, D. E. J. G. J.; Fukumura, D.; Jain, R. K. Photodynamic Therapy for Cancer. *Nat. Rev. Cancer* **2003**, *3* (5), 380–387. https://doi.org/10.1038/nrc1071.

(2)   Agostinis, P.; Berg, K.; Cenge, K. A.; Foster, T. H.; Girotti, A. W.; Gollnick, S. O.; Hahn, S. M.; Hamblin, M. R.; Juzeniene, A.; Kessel, D.; Korbelik, M.; Moan, J.; Mroz, P.; Nowis, D.; Piette, J.; Wilson, B. C.; Golab, J. Photodynamic Therapy of Cancer: An Update. *Ca Cancer J Clin* **2017**, *61* (April), 250–281. https://doi.org/10.3322/caac.20114.Available.

(3)   Anand, S.; Ortel, B. J.; Pereira, S. P.; Hasan, T.; Maytin, E. V. Biomodulatory Approaches to Photodynamic Therapy for Solid Tumors. *Cancer Lett.* **2012**, *326* (1), 8–16. https://doi.org/10.1016/j.canlet.2012.07.026.

(4)   Tsai, M. F.; Chang, S. H. G.; Cheng, F. Y.; Shanmugam, V.; Cheng, Y. S.; Su, C. H.; Yeh, C. S. Au Nanorod Design as Light-Absorber in the First and Second Biological

Near-Infrared Windows for *in Vivo* Photothermal Therapy. *ACS Nano* **2013**, *7* (6), 5330–5342. https://doi.org/10.1021/nn401187c.

(5)   Cao, J.; Zhu, B.; Zheng, K.; He, S.; Meng, L.; Song, J.; Yang, H. Recent Progress in NIR-II Contrast Agent for Biological Imaging. *Front. Bioeng. Biotechnol.* **2020**, *7* (January), 1–21. https://doi.org/10.3389/fbioe.2019.00487.

(6)   Lane, L. A.; Xue, R.; Nie, S. Emergence of Two Near-Infrared Windows for *in Vivo* and Intraoperative SERS. *Curr. Opin. Chem. Biol.* **2018**, *45* (April), 95–103. https://doi.org/10.1016/j.cbpa.2018.03.015.

(7)   Hashizume, H.; Baluk, P.; Morikawa, S.; McLean, J. W.; Thurston, G.; Roberge, S.; Jain, R. K.; McDonald, D. M. Openings between Defective Endothelial Cells Explain Tumor Vessel Leakiness. *Am. J. Pathol.* **2000**, *156* (4), 1363–1380. https://doi.org/10.1016/S0002-9440(10)65006-7.

(8)   Hu, L.; Zhang, C.; Zeng, G.; Chen, G.; Wan, J.; Guo, Z.; Wu, H.; Yu, Z.; Zhou, Y.; Liu, J. Metal-Based Quantum Dots: Synthesis, Surface Modification, Transport and Fate in Aquatic Environments and Toxicity to Microorganisms. *RSC Adv.* **2016**, *6* (82), 78595–78610. https://doi.org/10.1039/c6ra13016j.

(9)   Kim, H. S.; Lee, D. Y. Near-Infrared-Responsive Cancer Photothermal and Photodynamic Therapy Using Gold Nanoparticles. *Polymers (Basel).* **2018**, *10* (9), 1–14. https://doi.org/10.3390/polym10090961.

(10)   Pu, K. Y.; Liu, B. Optimizing the Cationic Conjugated Polymer-Sensitized Fluorescent Signal of Dye Labeled Oligonucleotide for Biosensor Applications. *Biosens. Bioelectron.* **2009**, *24* (5), 1067–1073. https://doi.org/10.1016/j.bios.2008.07.029.

(11)   Kilin, V. N.; Anton, H.; Anton, N.; Steed, E.; Vermot, J.; Vandamme, T. F.; Mely, Y.; Klymchenko, A. S. Counterion-Enhanced Cyanine Dye Loading into Lipid Nano-Droplets for Single-Particle Tracking in Zebrafish. *Biomaterials* **2014**, *35* (18), 4950–4957. https://doi.org/10.1016/j.biomaterials.2014.02.053.

(12)   Duan, X.; Liu, L.; Feng, F.; Wang, S. Cationic Conjugated Polymers for Optical Detection of DNA Methylation, Lesions, and Single Nucleotide Polymorphisms. *Acc. Chem. Res.* **2010**, *43* (2), 260–270. https://doi.org/10.1021/ar9001813.

(13)   Wu, C.; Chiu, D. T. Highly Fluorescent Semiconducting Polymer Dots for Biology and Medicine. *Angew. Chemie - Int. Ed.* **2013**, *52* (11), 3086–3109. https://doi.org/10.1002/anie.201205133.

(14)   Zhu, C.; Liu, L.; Yang, Q.; Lv, F.; Wang, S. Water-Soluble Conjugated Polymers for Imaging, Diagnosis, and Therapy. *Chem. Rev.* **2012**, *112* (8), 4687–4735. https://doi.org/10.1021/cr200263w.

(15)   Kuehne, A. J. C. Conjugated Polymer Nanoparticles toward *in Vivo* Theranostics – Focus on Targeting, Imaging, Therapy, and the Importance of Clearance. *Adv. Biosyst.* **2017**, *1* (11), 1700100. https://doi.org/10.1002/adbi.201700100.

(16)   Li, K.; Liu, B. Polymer Encapsulated Conjugated Polymer Nanoparticles for Fluorescence Bioimaging. *J. Mater. Chem.* **2012**, *22* (4), 1257–1264. https://doi.org/10.1039/c1jm14397b.

(17)   Abelha, T. F.; Dreiss, C. A.; Green, M. A.; Dailey, L. A.; Abelha, T. F. Conjugated Polymers as Nanoparticle Probes for Fluorescence and Photoacoustic Imaging. *J. Mater. Chem. B* **2020**, *8* (4), 592–606. https://doi.org/10.1039/c9tb02582k.

(18)   Rohatgi, C. V.; Harada, T.; Need, E. F.; Krasowska, M.; Beattie, D. A.; Dickenson, G. D.; Smith, T. A.; Kee, T. W. Low-Bandgap Conjugated Polymer Dots for Near-Infrared Fluorescence Imaging. *ACS Appl. Nano Mater.* **2018**, *1* (9), 4801–4808. https://doi.org/10.1021/acsanm.8b01014.

(19)   Feng, G.; Fang, Y.; Liu, J.; Geng, J.; Ding, D.; Liu, B. Multifunctional Conjugated Polymer Nanoparticles for Image-Guided Photodynamic and Photothermal Therapy. *Small* **2017**, *13* (3), 1–12. https://doi.org/10.1002/smll.201602807.

(20)   Yuan, H.; Wang, B.; Lv, F.; Liu, L.; Wang, S. Conjugated-Polymer-Based Energy-Transfer Systems for Antimicrobial and Anticancer Applications. *Adv. Mater.* **2014**, *26* (40), 6978–6982. https://doi.org/10.1002/adma.201400379.

(21)   Gesquiere, A. J.; Jasmin, K.; Topps, M.; Shroff, S.; Ortiz, A. M.; George, O.; Abdellatif, Y.; Ortiz Ortiz, A. M.; Abdellatif, Y. Conjugated Polymer Nanotherapeutics for Next Generation Photodynamic Therapy. *Med. Res. Arch.* **2018**, *6* (2), 23.

(22)   Manandhar, S.; Sjöholm, E.; Bobacka, J.; Rosenholm, J. M.; Bansal, K. K. Polymer-Drug Conjugates as Nanotheranostic Agents. *J. Nanotheranostics* **2021**, *2* (1), 63–81. https://doi.org/10.3390/jnt2010005.

(23)   Wang, C.; Zhang, W.; Meng, X.; Bergqvist, J.; Liu, X.; Genene, Z.; Xu, X.; Yartsev, A.; Inganäs, O.; Ma, W.; Wang, E.; Fahlman, M. Ternary Organic Solar Cells with Minimum Voltage Losses. *Adv. Energy Mater.* **2017**, *7* (21), 1700390. https://doi.org/10.1002/aenm.201700390.

(24)   Soon, Y. W.; Cho, H.; Low, J.; Bronstein, H.; Mc Cullocha, I.; Durrant, J. R. Correlating Triplet Yield, Singlet Oxygen Generation and Photochemical Stability in Polymer/Fullerene Blend Films. *Chem. Commun.* **2013**, *49* (13), 1291–1293.

https://doi.org/10.1039/c2cc38243a.

(25)   Wu, C.; Szymanski, C.; McNeill, J. Preparation and Encapsulation of Highly Fluorescent Conjugated Polymer Nanoparticles. *Langmuir* **2006**, *22* (7), 2956–2960. https://doi.org/10.1021/la060188l.

(26)   Brown, W.; Schillén, K.; Almgren, M.; Hvidt, S.; Bahadur, P. Micelle and Gel Formation in a Poly(ethylene Oxide)/Poly(propylene Oxide)/ Poly(ethylene Oxide) Triblock Copolymer in Water Solution. Dynamic and Static Light Scattering and Oscillatory Shear Measurements. *J. Phys. Chem.* **1991**, *95* (4), 1850–1858. https://doi.org/10.1021/j100157a064.

(27)   Abelha, T. F.; Neumann, P. R.; Holthof, J.; Dreiss, C. A.; Alexander, C.; Green, M.; Dailey, L. A. Low Molecular Weight PEG-PLGA Polymers Provide a Superior Matrix for Conjugated Polymer Nanoparticles in Terms of Physicochemical Properties, Biocompatibility and Optical/Photoacoustic Performance. *J. Mater. Chem. B* **2019**, *7* (33), 5115–5124. https://doi.org/10.1039/c9tb00937j.

(28)   Hoshyar, N.; Gray, S.; Han, H.; Bao, G. The Effect of Nanoparticle Size on *in Vivo* Pharmacokinetics and Cellular Interaction. *Nanomedicine* **2016**, *11* (6), 673–692. https://doi.org/10.2217/nnm.16.5.

(29)   Guo, X.; Wu, Z.; Li, W.; Wang, Z.; Li, Q.; Kong, F.; Zhang, H.; Zhu, X.; Du, Y. P.; Jin, Y.; Du, Y.; You, J. Appropriate Size of Magnetic Nanoparticles for Various Bioapplications in Cancer Diagnostics and Therapy. *ACS Appl. Mater. Interfaces* **2016**, *8* (5), 3092–3106. https://doi.org/10.1021/acsami.5b10352.

(30)   Nagayama, S.; Ogawara, K. ichi; Fukuoka, Y.; Higaki, K.; Kimura, T. Time-Dependent Changes in Opsonin Amount Associated on Nanoparticles Alter Their Hepatic Uptake

Characteristics. *Int. J. Pharm.* **2007**, *342* (1–2), 215–221. https://doi.org/10.1016/j.ijpharm.2007.04.036.

(31)   Bencheikh, F.; Duché, D.; Ruiz, C. M.; Simon, J. J.; Escoubas, L. Study of Optical Properties and Molecular Aggregation of Conjugated Low Band Gap Copolymers: PTB7 and PTB7-Th. *J. Phys. Chem. C* **2015**, *119* (43), 24643–24648. https://doi.org/10.1021/acs.jpcc.5b07803.

(32)   Spano, F. C.; Silva, C. H- and J-Aggregate Behavior in Polymeric Semiconductors. *Annu. Rev. Phys. Chem.* **2014**, *65* (1), 477–500. https://doi.org/10.1146/annurev-physchem-040513-103639.

(33)   Ito, M.; Palanisamy, K.; Kumar, A.; Murugesan, V. S.; Shin, P. K.; Tsuda, N.; Yamada, J.; Ochiai, S. Characterization of the Organic Thin Film Solar Cells with Active Layers of PTB7/PC71BM Prepared by Using Solvent Mixtures with Different Additives. *Int. J. Photoenergy* **2014**, *vol. 2014,* Article ID 694541, 8 pages. https://doi.org/10.1155/2014/694541.

(34)   Demas, J. N.; Crosby, G. A. The Measurement of Photolumineseence Quantum Yields. A Review. *J. Phys. Chem.* **1971**, *75* (8), 991–1024. https://doi.org/10.1021/j100678a001.

(35)   Hedley, G. J.; Ward, A. J.; Alekseev, A.; Howells, C. T.; Martins, E. R.; Serrano, L. A.; Cooke, G.; Ruseckas, A.; Samuel, I. D. W. Determining the Optimum Morphology in High-Performance Polymer-Fullerene Organic Photovoltaic Cells. *Nat. Commun.* **2013**, *4,* 2867. https://doi.org/10.1038/ncomms3867.

(36)   Crossley, D. L.; Urbano, L.; Neumann, R.; Bourke, S.; Jones, J.; Dailey, L. A.; Green, M.; Humphries, M. J.; King, S. M.; Turner, M. L.; Ingleson, M. J. Post-Polymerization

C-H Borylation of Donor-Acceptor Materials Gives Highly Efficient Solid State Near-Infrared Emitters for Near-IR-OLEDs and Effective Biological Imaging. *ACS Appl. Mater. Interfaces* **2017**, *9* (34), 28243–28249. https://doi.org/10.1021/acsami.7b08473.

(37) Wang, S.; Gao, R.; Zhou, F.; Selke, M. Nanomaterials and Singlet Oxygen Photosensitizers: Potential Applications in Photodynamic Therapy. *J. Mater. Chem.* **2004**, *14*, 487–493. https://doi.org/10.1039/b311429e.

(38) Plaetzer, K.; Krammer, B.; Berlanda, J.; Berr, F.; Kiesslich, T. Photophysics and Photochemistry of Photodynamic Therapy: Fundamental Aspects. *Lasers Med. Sci.* **2009**, *24* (2), 259–268. https://doi.org/10.1007/s10103-008-0539-1.

(39) Gorman, A. A.; Rodgers, M. A. J. Singlet Molecular Oxygen. *Chem. Soc. Rev.* **1981**, *10*, 205–231. https://doi.org/10.1016/0026-265x(78)90048-6.

(40) Kim, S.; Rashid, M. A. M.; Ko, T.; Ahn, K.; Shin, Y.; Nah, S.; Kim, M. H.; Kim, B. S.; Kwak, K.; Cho, M. New Insights into the Photodegradation Mechanism of the PTB7-Th Film: Photooxidation of π-Conjugated Backbone upon Sunlight Illumination. *J. Phys. Chem. C* **2020**, *124* (5), 2762–2770. https://doi.org/10.1021/acs.jpcc.9b09954.

(41) Salvador, M.; Gasparini, N.; Perea, J. D.; Paleti, S. H.; Distler, A.; Inasaridze, L. N.; Troshin, P. A.; Lüer, L.; Egelhaaf, H. J.; Brabec, C. Suppressing Photooxidation of Conjugated Polymers and Their Blends with Fullerenes through Nickel Chelates. *Energy Environ. Sci.* **2017**, *10* (9), 2005–2016. https://doi.org/10.1039/c7ee01403a.

(42) Lin, H.; Shen, Y.; Chen, D.; Lin, L.; Wilson, B. C.; Li, B.; Xie, S. Feasibility Study on Quantitative Measurements of Singlet Oxygen Generation Using Singlet Oxygen Sensor Green. *J. Fluoresc.* **2013**, *23* (1), 41–47. https://doi.org/10.1007/s10895-012-1114-5.

(43)   Matheson, I. B. C.; Lee, J.; King, A. D. The Lifetime of Singlet Oxygen (1Δg) in Heavy Water, a Revised Value. *Chem. Phys. Lett.* **1978**, *55* (1), 49–51. https://doi.org/https://doi.org/10.1016/0009-2614(78)85129-X.

(44)   Lindig, B. A.; Rodgers, M. A. J.; Schaaplc, A. P. Determination of the Lifetime of Singlet Oxygen in D20 Using 9,10-Anthracenedipropionic Acid, a Water-Soluble Probe. *J. Am. Chem. Soc.* **1980**, *102* (17), 5590–5593. https://doi.org/10.1021/ja00537a030.

(45)   Sáenz-Trevizo, A.; Pizá-Ruiz, P.; Chávez-Flores, D.; Ogaz-Parada, J.; Amézaga-Madrid, P.; Vega-Ríos, A.; Miki-Yoshida, M. On the Discoloration of Methylene Blue by Visible Light. *J. Fluoresc.* **2019**, *29* (1), 15–25. https://doi.org/10.1007/s10895-018-2304-6.

(46)   Wei, Z.; Xue, F.; Xin, F.; Wu, M.; Wang, B.; Zhang, X.; Yang, S.; Guo, Z.; Liu, X. A Thieno-Isoindigo Derivative-Based Conjugated Polymer Nanoparticle for Photothermal Therapy in the NIR-II Bio-Window. *Nanoscale* **2020**, *12* (38), 19665–19672. https://doi.org/10.1039/d0nr03771k.

(47)   Guo, B.; Sheng, Z.; Kenry; Hu, D.; Lin, X.; Xu, S.; Liu, C.; Zheng, H.; Liu, B. Biocompatible Conjugated Polymer Nanoparticles for Highly Efficient Photoacoustic Imaging of Orthotopic Brain Tumors in the Second Near-Infrared Window. *Mater. Horizons* **2017**, *4* (6), 1151–1156. https://doi.org/10.1039/c7mh00672a.

(48)   Calzoni, E.; Cesaretti, A.; Polchi, A.; Di Michele, A.; Tancini, B.; Emiliani, C. Biocompatible Polymer Nanoparticles for Drug Delivery Applications in Cancer and Neurodegenerative Disorder Therapies. *J. Funct. Biomater.* **2019**, *10* (1), 1–15. https://doi.org/10.3390/jfb10010004.

(49)   Meng, Z.; Hou, W.; Zhou, H.; Zhou, L.; Chen, H.; Wu, C. Therapeutic Considerations

and Conjugated Polymer-Based Photosensitizers for Photodynamic Therapy. *Macromol. Rapid Commun.* **2018**, *39* (5), 1–15. https://doi.org/10.1002/marc.201700614.

(50) Chen, Y.; Azad, M. B.; Gibson, S. B. Superoxide Is the Major Reactive Oxygen Species Regulating Autophagy. *Cell Death Differ.* **2009**, *16* (7), 1040–1052. https://doi.org/10.1038/cdd.2009.49.

(51) Buccellato, L. J.; Tso, M.; Akinci, O. I.; Chandel, N. S.; Budinger, G. R. S. Reactive Oxygen Species Are Required for Hyperoxia-Induced Bax Activation and Cell Death in Alveolar Epithelial Cells. *J. Biol. Chem.* **2004**, *279* (8), 6753–6760. https://doi.org/10.1074/jbc.M310145200.

(52) Manning, P.; McNeil, C. J.; Cooper, J. M.; Hillhouse, E. W. Direct, Real-Time Sensing of Free Radical Production by Activated Human Glioblastoma Cells. *Free Radic. Biol. Med.* **1998**, *24* (97), 1304–1309.

(53) Manning, P.; Cookson, M. R.; McNeil, C. J.; Figlewicz, D.; Shaw, P. J. Superoxide-Induced Nitric Oxide Release from Cultured Glial Cells. *Brain Res.* **2001**, *911* (2), 203–210. https://doi.org/10.1016/S0006-8993(01)02688-9.

(54) Boulton, S. J.; Keane, P. C.; Morris, C. M.; McNeil, C. J.; Manning, P. Real-Time Monitoring of Superoxide Generation and Cytotoxicity in Neuroblastoma Mitochondria Induced by 1-Trichloromethyl- 1,2,3,4-Tetrahydro-Beta-Carboline. *Redox Rep.* **2012**, *17* (3), 108–114. https://doi.org/10.1179/1351000212Y.0000000011.

(55) Oda, T.; Maeda, H. Binding to and Internalization by Cultured Cells of Neocarzinostatin and Enhancement of Its Actions by Conjugation with Lipophilic Styrene-Maleic Acid Copolymer. *Cancer Res.* **1987**, *47* (12), 3206–3211.

(56) Guller, A. E.; Generalova, A. N.; Petersen, E. V.; Nechaev, A. V.; Trusova, I. A.; Landyshev, N. N.; Nadort, A.; Grebenik, E. A.; Deyev, S. M.; Shekhter, A. B.; Zvyagin, A. V. Cytotoxicity and Non-Specific Cellular Uptake of Bare and Surface-Modified Upconversion Nanoparticles in Human Skin Cells. *Nano Res.* **2015**, *8* (5), 1546–1562. https://doi.org/10.1007/s12274-014-0641-6.

(57) Blanco, E.; Shen, H.; Ferrari, M. Principles of Nanoparticle Design for Overcoming Biological Barriers to Drug Delivery. *Nat. Biotechnol.* **2015**, *33* (9), 941–951. https://doi.org/10.1038/nbt.3330.

(58) Chen, Y.; Zhang, W.; Huang, Y.; Gao, F.; Sha, X.; Lou, K.; Fang, X. The Therapeutic Effect of Methotrexate-Conjugated Pluronic-Based Polymeric Micelles on the Folate Receptor-Rich Tumors Treatment. *Int. J. Nanomedicine* **2015**, *10*, 4043–4057. https://doi.org/10.2147/IJN.S79045.

(59) Pitto-Barry, A.; Barry, N. P. E. Pluronic® Block-Copolymers in Medicine: From Chemical and Biological Versatility to Rationalisation and Clinical Advances. *Polym. Chem.* **2014**, *5* (10), 3291–3297. https://doi.org/10.1039/c4py00039k.

(60) Akash, M. S. H.; Rehman, K. Recent Progress in Biomedical Applications of Pluronic (PF127): Pharmaceutical Perspectives. *J. Control. Release* **2015**, *209*, 120–138. https://doi.org/10.1016/j.jconrel.2015.04.032.

(61) Russo, A.; Pellosi, D. S.; Pagliara, V.; Milone, M. R.; Pucci, B.; Caetano, W.; Hioka, N.; Budillon, A.; Ungaro, F.; Russo, G.; Quaglia, F. Biotin-Targeted Pluronic® P123/F127 Mixed Micelles Delivering Niclosamide: A Repositioning Strategy to Treat Drug-Resistant Lung Cancer Cells. *Int. J. Pharm.* **2016**, *511* (1), 127–139. https://doi.org/10.1016/j.ijpharm.2016.06.118.

(62) Wang, H.; Zhang, F.; Wen, H.; Shi, W.; Huang, Q.; Huang, Y.; Xie, J.; Li, P.; Chen, J.; Qin, L.; Zhou, Y. Tumor- and Mitochondria-Targeted Nanoparticles Eradicate Drug Resistant Lung Cancer through Mitochondrial Pathway of Apoptosis. *J. Nanobiotechnology* **2020**, *18* (1), 1–21. https://doi.org/10.1186/s12951-019-0562-3.